



Correlation between theoretical descriptor and catalytic oxygen reduction activity of graphene supported palladium and palladium alloy electrocatalysts



Min Ho Seo ^a, Sung Mook Choi ^b, Dong Un Lee ^a, Won Bae Kim ^{b,*,**}, Zhongwei Chen ^{a,*}

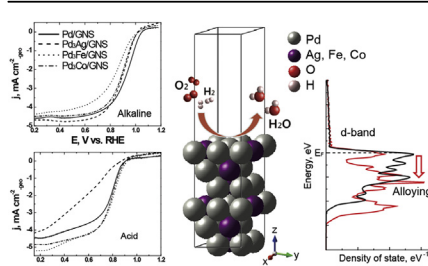
^a Department of Chemical Engineering, Waterloo Institute for Nanotechnology, Waterloo Institute of Sustainable Energy, University of Waterloo, 200 University Ave. W, Waterloo, ON, N2L 3G1, Canada

^b School of Materials Science and Engineering, Gwangju Institute of Science and Technology (GIST), 261 Cheomdan-gwagiro, Gwangju, 500-712, South Korea

HIGHLIGHTS

- Highly dispersed Pd and Pd alloy nanoparticles on graphene at loadings up to 60 wt.%.
- The experimental measurements of Pd3d core level with DFT calculation.
- Identifying the d band center of Pd atom in the Pd and Pd₃X alloy by DFT calculation.
- A descriptor for ORR activity by the electronic structure of bimetallic Pd alloys.
- A fundamental relationship on Pd and Pd alloy for ORR in acidic and alkaline media.

GRAPHICAL ABSTRACT



ARTICLE INFO

Article history:

Received 20 April 2015

Received in revised form

21 July 2015

Accepted 22 August 2015

Available online 24 September 2015

Keywords:

Oxygen reduction reaction

Palladium

Graphene

Electrocatalyst

Density functional theory

Dissolution potential

ABSTRACT

The oxygen reduction reaction, ORR, performances of graphene-supported palladium (Pd) and palladium alloys (Pd₃X: X = Ag, Co and Fe) catalysts with highly dispersed catalyst particles are investigated in acidic and alkaline conditions using a rotating disk electrode, RDE. Graphene nanosheet, GNS, supported Pd based catalysts are fabricated without surfactant through the impregnation of Pd and 2nd metal precursors on GNS, leading to small and uniformly dispersed nanoparticles, even when high metal loading of up to 60 wt.% are deposited on supports. The ab-initio density functional theory, DFT, calculations, which are based on the d-band center theory, have been applied to correlate with the results of the ORR performances obtained by half-cell tests. Additionally, the cohesive energy, E_{coh} , and dissolution potential, U_m , for the Pd nanoparticles have been calculated to understand thermodynamic stability. To elucidate the d-band center shift, the Pd 3d_{5/2} core-level binding energies for Pd/GNS, Pd₃Ag/GNS, Pd₃Fe/GNS and Pd₃Co/GNS have been investigated by X-ray photoelectron spectroscopy, XPS. The GNS-supported Pd, or Pd-based alloy-nanoparticle catalyst shows good ORR activity under acidic and alkaline conditions, suggesting it may offer potential replacement for Pt for use in cathode electrodes of anion-exchange membrane fuel cell, AEMFC, and acid based polymer electrolyte fuel cell, PEMFC.

© 2015 Elsevier B.V. All rights reserved.

* Corresponding author.

** Corresponding author.

E-mail addresses: wbkim@gist.ac.kr (W.B. Kim), zhwchen@uwaterloo.ca (Z. Chen).

1. Introduction

Fuel cells are one of the most promising energy conversion devices to eventually replace classical fossil-fuel-based power sources [1,2]. The system utilizes electrochemical reactions to convert the chemical energy of fuel into electricity, which leads to higher efficiency than combustion engines [1,2]. The acid-based polymer electrolyte membrane fuel cells, PEMFCs, and anion-exchange membrane fuel cell, AEMFC, have gained attention due to their broad range of power production requirements at low temperatures (<100 °C) [1]. Employing PEMFC, however, faces several obstacles, primarily the sluggish kinetics of the oxygen reduction reaction, ORR, and thermodynamic instability of cathodes under harsh electrochemical conditions [1,3,4]. For these reasons, Pt based catalysts have been the exclusive choice as they demonstrate both acceptable activity and stability [1,5]. However for future implementation of Pt based catalysts, the obstacles of high price and limited supply of the electrode materials (i.e., Pt-based materials) must be addressed. Accordingly, various approaches have been made in effort not only to reduce Pt content in fuel cell electrocatalysts [6–10], but also to replace it with non-Pt materials to lower the cost while maintaining high ORR activity [11–14]. In particular, Pd based catalysts have been shown as potential ORR electrocatalyst without the use of Pt. Even in AFCs, which being into interest again with the development of solid type anion exchange membrane, AEM, Pd and Ag based catalysts are utilized instead of conventional Pt catalysts as cathode materials for ORR [11,15–18]. The activity of Pd catalysts is comparable to that of state-of-the-art Pt nanoparticle supported on carbon electrocatalysts in acidic conditions [19–22]. Pd is not only around five times lower in price than Pt but is also more thermodynamically stable than other transition metals such as Ni, Co, Fe and Cu [23–26]. From previous literature, Pd and Pd alloys electrocatalysts have been reported to be especially effective for the ORR under alkaline conditions [27,28]. We have also previously demonstrated that the catalyst of highly concentrated Pd nanoparticles supported on GNS can show the higher ORR activity than GNS supported Pt [11].

For their applications in fuel cells, support materials are employed to facilitate deposition of metal nanoparticles to obtain high active surface area and stability. The support materials need to satisfy specific properties such as electrochemical stability under the fuel cells operating condition, sufficient porosity for smooth gas flow, high electrical conductivity to assist the progress of electron pathway, and sufficient surface area to allow high metal dispersion [29]. The performance of a fuel cell depends to a large extent on the size and dispersion of the metal nanoparticles in its electrodes. Graphene nanosheets have superior chemical and physical properties, such as extremely large surface area of ca. 2630 m² g⁻¹ [30], chiral quantum hall effects [31,32], high electronic and thermal conductivity [33], and high mechanical strength [34]. On the other hand, the commercial amorphous carbon such as Vulcan XC-72R, which is one of the most popular catalysts supports for fuel cell applications, has lower surface area of 300 m² g⁻¹ [35,36] as well as it exhibits a high density of surface defects on edges and corners of basal planes, where carbon oxidation reaction can take place since the oxidation starts at the defect sites at normal high operating potentials [36,37]. The support oxidation of less defected GNSs can be suppressed, retaining its base graphitic nature [38]. Having said this, we have previously reported numerous metal-supported GNS catalysts even with metal loadings above 60 wt.%, taking advantages of properties of GNS [4,7,11,39–41].

Since the first report of the d-band center model from Nørskov and co-workers, which was calculated using density functional theory, DFT [42,43], the field of fuel cell catalysts has been

driving research toward theoretical predictions of surface reactivity and toward experimental substantiation of such predictions [20,44–47]. According to these authors, the center of the d-band of catalysts is strongly related to the changes in the catalyst surface bond energy and the species adsorbed on the surface (e.g., oxygen, hydrogen and methanol) [23,42,45,47]. The upper weight position of the d-band with respect to the Fermi level indicates stronger interactions with adsorbates such as oxygen [20,44–47]. Even Pt exhibits interactions that are too strong for O adsorption; thus, the low-lying d-band center of Pt on the surface of Pt alloy demonstrates faster kinetics than the Pt alone because of the larger vacancy of the d-band of Pt, which suggests a weaker Pt–O bond [44–47]. Moreover, Pd exhibits stronger interactions with oxygen at a fast kinetic rate for the breaking of O–O bonds than those exhibited by oxygen bond making, which indicates slower kinetics for the ORR [20]. Therefore, the modification of the d-band center for Pt or Pd through the formation of alloys with second metals could predict the kinetics of the ORR. There are several theoretical prediction reports for ORR using DFT over some catalyst alloys with compositions of Pt₃X or Pd₃X (X = Ni, Co, Fe, Au, Ir, etc.) by using d-band center model [47].

The goal of this work is to elucidate the ORR reactivity on Pd alloys by inducing a shift of the d-band center under both acidic and alkaline conditions. In order to allow the identification of an alloy with calculated d-band center, GNS is employed for the deposition of Pd₃X (X = Ag, Co and Fe) metal nanoparticles. The GNS-supported Pd₃X catalysts are fabricated through the impregnation method without the use of surfactant caused by heat treatment of Pd and other metal precursors in GNSs in hydrogen atmosphere. Pd-based catalysts on GNSs are used to experimentally substantiate the theoretical predictions of Pd₃X as the ORR catalysts in both acidic and alkaline solutions. The ORR activities of GNS-supported Pd₃X catalysts with highly dispersed catalyst particles are investigated by using rotating disk electrode (RDE) technique. The ab initio DFT calculations have been conducted to correlate between the experimental results of the half-cell ORR electrochemical testing with the computational d-band values. The X-ray photoelectron spectroscopy (XPS), transmission electron microscopy (TEM) and X-ray diffraction (XRD) analyses are used to investigate the particle size, size distribution, and structural and electronic properties of the prepared materials. In ab-initio computational calculation, additionally, a dissolution potential and cohesive energy of Pd nanoparticle are calculated to understand thermodynamic stability in acidic and alkaline conditions.

2. Experimental

2.1. Synthesis of Pd and Pd₃X nanoparticles on GNSs

GNS was synthesized in accordance with the method described in the previous literature [11,40,48]. Natural graphite (Carbonix, Korea) was pre-oxidized in an oxidizing solution of phosphorus pentoxide (P₂O₅, Aldrich), potassium persulfate (K₂S₂O₈, Aldrich) and sulfuric acid (H₂SO₄, Aldrich) under vigorous stirring at 80 °C for 30 min. Then, the solution was diluted and filtered with de-ionized (DI) water (18 MΩ cm). Potassium permanganate (KMnO₄, Aldrich) was slowly put into the pre-oxidized graphite mixed with sulfuric acid, then DI water (350 ml) with hydrogen peroxide (30% H₂O₂, Aldrich) was added. The resulting mixture was thoroughly washed by centrifugation with a solution of hydrochloric acid (30% HCl, Aldrich) and DI water. Using pretreated dialysis tubing cellulose membrane (Aldrich), the dispersed graphite oxide, GO was subjected to dialysis for two weeks until the pH became neutral, allowing removal of ions, residual salts, and acids. Afterward, the GO was dried by freeze-drying. The

synthesized GO was treated by thermal exfoliation at 1103 K in a quartz tube furnace under Ar atmosphere for 60 s to obtain functionalized GNSs.

Pd and Pd₃X nanoparticles on GNS were synthesized by the impregnation method through a heat treatment under hydrogen gas [7,10]. The Pd salt (Pd(NO₃)₂·nH₂O, KOJIMA Chemicals) was mixed with salts of the second metal, i.e., Ag (AgNO₃, Aldrich), Fe (FeCl₃·6H₂O, Aldrich), and Co (CoCl₂·6H₂O, Aldrich), with the GNS material dispersed in acetone. The solution was stirred with a vortex mixer and ultrasonicated. The atomic molar ratio of Pd and the second metal was 3:1 (Pd₃X). In a convection oven, the solution was dried at 373 K for 10 h in order to allow evaporation of acetone, then the mixture was heat-treated with 4% H₂ in N₂ gas at 573 K for 3 h.

2.2. Physicochemical analyses of Pd₃X/GNS

To prepare the sample for TEM analysis, Pd/GNS and Pd₃X/GNS were dispersed in ethanol solution by ultrasonication prior to being dropped onto the standard Cu grid (200 mesh). The TEM (JEOL JEM-2100) was operated at 200 kV. The crystalline characteristics of Pd and its alloys were investigated by XRD (Rigaku Rotaflex, RU-200B) equipped with a Cu Kα (λ = 1.5405 Å) source. The XRD was operated at 10 kV and 10 mA, and the 2θ angular region from 30° to 90° was scanned at a rate of 1° min⁻¹. In order to investigate the surface composition and chemical states of Pd/GNS and Pd₃X/GNS, XPS (ESCALAB 250, UK) with Al Kα X-ray source (E = 1486.6 eV) was utilized. The results were processed by XPSPEAK software after correcting with the binding energy (BE, 284.5 eV) of the C 1s peak used as an internal standard. The background was fitted by the Shirley method.

2.3. Electrochemical characterization

The half-cell system was made up of well-polished glassy carbon (0.196 cm²) as working electrode (WE), a platinum-wire as counter electrode, CE, and double-junction Ag/AgCl (3 M KCl) and Hg/HgO/OH⁻ (MMO) for 0.1 M HClO₄ and 0.1 M NaOH electrolyte as reference electrode, RE, respectively. Catalyst slurry was prepared as follows: Pd/GNS and Pd₃X/GNS catalysts were dispersed in a solution of isopropyl alcohol, DI water with Nafion[®] ionomer solution (5 wt.%), then sonicated for 30 min. The WE was prepared by the thin-film electrode method [49,50]. The metal loading on a GC electrode (5 mm diameter) was determined to be 40 μg cm⁻² for both of Pd/GNS and Pd₃X/GNS catalysts.

The cyclic voltammograms, CVs and ORR polarization curves were obtained in an N₂ and O₂-saturated 0.1 M NaOH or 0.1 M HClO₄ solution at room temperature by using Solartron cell test system (AMETEK model 1470E). The polarization curves using RDE in 0.1 M NaOH and 0.1 M HClO₄ saturated with O₂ gas at 298 K were obtained using a sweep rate of 10 mV s⁻¹ in the potential range of 1.2 to 0.1 V vs. RHE. The experimentally obtained limited diffusion current density (j_d) was plotted at the selected rotation speed. The polarization curves of Pd/GNS and Pd₃X/GNS with respect to ORR were obtained at rotating speeds of 400, 900, 1600 and 2500 rpm in O₂-saturated 0.1 M NaOH and 0.1 M HClO₄ solutions. All potentials were measured with reference to the reversible hydrogen electrode (RHE).

2.4. Computational detail

The total energies of Pd, Pd alloys and Pd nanoparticles were calculated by using the Vienna ab initio simulation package, VASP program [51] with the implemented DFT method [52,53]. The pseudo-potentials through the projector augmented wave (PAW)

method were used to replace the interaction potential of the core electrons [54,55]. The Perdew, Burke and Ernzerhof (PBE) functional was used to describe the electron exchange-correlation energy [56], employing the spin-polarized generalized gradient approximation (GGA) [57,58]. The valence electrons expressed by Kohn-Sham wave functions were expanded with a plane-wave basis set. A gamma point mesh with (25 × 25 × 25) k-points was used for the Pd and Pd₃X unit cell to sample the Brillouin zone for bulk calculation. Regarding nanoparticle calculation, a gamma point mesh was run with (1 × 1 × 1) k-points imposed in a vacuum space which was twice as big as the particle size. The energies were cut off at 326 eV. During optimizing structural, all ions were fully relaxed until the internal energies were converged within 10⁻⁴ eV. To calculate DOS of surface, Pd and Pd₃X (111) surfaces were generated on the (2 × 2) unit cell, and a vacuum space of 20 Å was employed to avoid interactions between top and bottom surface. For calculation of the total energies of Pd and Pd alloy slab models, gamma point mesh of (25 × 25 × 1) and the Methfessel-Paxton smearing method [59] were utilized.

3. Results and discussion

3.1. Structural properties of GNS-supported Pd and Pd₃X nanoparticles

Possessing high surface areas and high loading of Pd and Pd₃X nanoparticles, the chemically synthesized GNSs display a sheet-like morphology as shown in inset Fig. 1a. The amorphous carbon black such as Vulcan XC-72R, which is a widely used support material, exhibits a rather lower surface area of ca. 300 m² g⁻¹ [35,36] and a high density of surface defects because of their heterogeneous structure produced by pyrolysis of liquid or hydrocarbons [38,60], whereas the GNSs have a higher surface area and fewer defect sites, retaining its base graphitic nature. The lower surface area of amorphous carbon black might not be enough to make homogeneously dispersed small nanoparticles at highly concentrated metal loading on the support, since not only the particle size tends to grow with increased metal concentration on the support [7,60–63] but also the metal is likely to sinter due to poor interactions between the carbon support and metal [61,62]. On the other hand, Fig. 1 demonstrates homogeneously distributed Pd and Pd alloy nanoparticles deposited on GNS even with loadings higher than 60 wt.% with a uniform metal particle size. Based on the TEM analysis, the morphology, average particle size and its distribution of Pd/GNS and Pd₃X/GNS are shown in Fig. 1 and Table 1. The average particle size was estimated by employing more than 150 visible different particles on the micrographs. The nanoparticle sizes of GNS-supported Pd, Pd₃Ag, Pd₃Co and Pd₃Fe are estimated to be ca. 4.2, 4.8, 3.4, and 4.2 nm, respectively (see Table 1).

The average crystallite sizes and lattice parameters for Pd/GNS, Pd₃Ag/GNS, Pd₃Co/GNS and Pd₃Fe/GNS are estimated using the angular position (2θ_{max}) and the full-width at half-maximum (FWHM) of the (220) diffraction peak obtained from XRD patterns as shown in Fig. 2. The (220) peak is employed as the reference to prevent possible disturbances from the peaks of GNS support [64]. The calculated crystallite sizes of Pd/GNS, Pd₃Ag/GNS, Pd₃Fe/GNS and Pd₃Co/GNS from the (220) peaks are ca. 5.7, 5.6, 4.6 and 4.5 nm, respectively. Since relatively larger particles mainly respond to the XRD signal, the average nanoparticle sizes obtained from the TEM analysis are smaller than those obtained from XRD [65]. The lattice constants of the catalysts are calculated also using the diffraction peak position at the (220). The lattice constants of Pd₃Co/GNS and Pd₃Fe/GNS are decreased due to the smaller atomic radius of Co and Fe relative to that of Pd. The lattice constant of Pd₃Ag/GNS is increased because of larger atomic radius of Ag. In

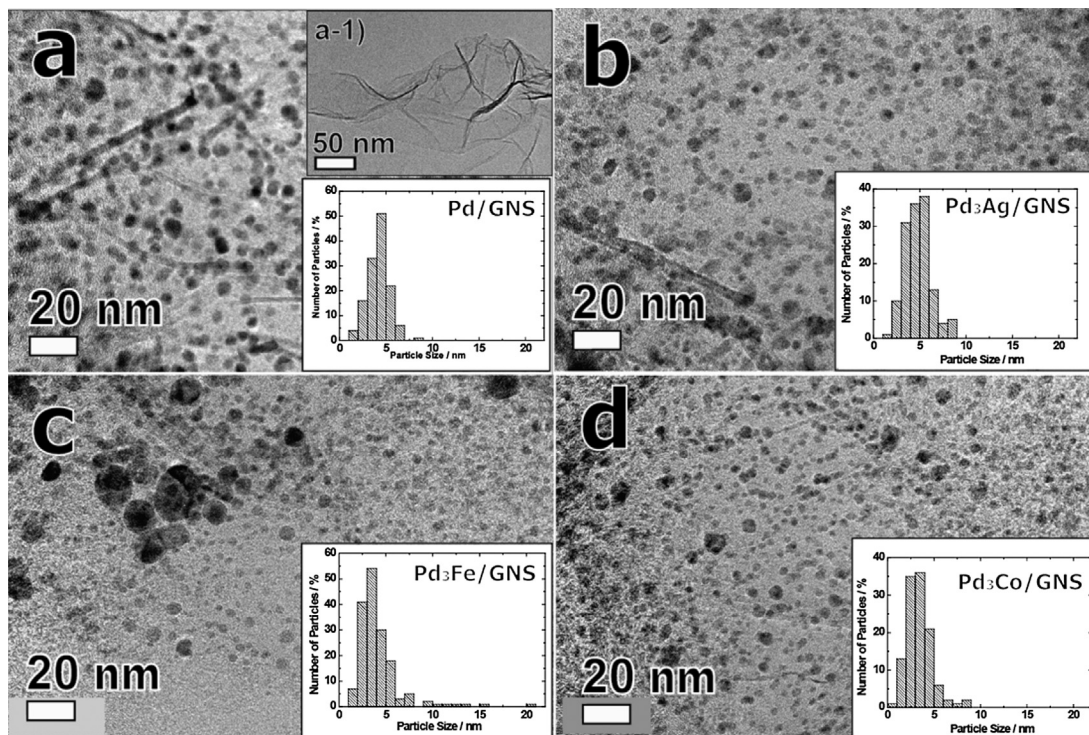


Fig. 1. TEM images of GNS-supported (a) Pd, (b) Pd₃Ag, (c) Pd₃Fe and (d) Pd₃Co with corresponding histograms of particle sizes. The inset figure (a–1) shows GNS.

Table 1
Physicochemical parameters and d-band center values (ϵ_d) of Pd and Pd₃X alloy (X: Ag, Fe and Co) catalyst supported on GNS from XRD, TEM, XPS analyses and DFT calculation.

Samples	Heat treatment temp. (K)	Lattice parameter ^a (nm)	TEM particle size ^b (nm)	XPS ^c		ϵ_d (eV)
				Pd 3d _{5/2} core level BE (eV)	Pd 3d _{3/2} core level BE (eV)	
60 wt.% Pd/GNS	573	0.389	4.19 ± 0.87	335.3	340.5	–1.82
67 wt.% Pd ₃ Ag/GNS	573	0.396	4.81 ± 1.1	335.2	340.5	–1.69
64 wt.% Pd ₃ Fe/GNS	573	0.388	4.21 ± 1.5	335.4	340.6	–2.21
64 wt.% Pd ₃ Co/GNS	573	0.386	3.40 ± 0.98	335.4	340.7	–2.15

^a Lattice parameter estimated from XRD measurement.

^b Average particle size of the nanoparticles evaluated by counting at least over 150 visible particles from TEM image.

^c The core level energy for Pd 3d_{5/2} and Pd 3d_{3/2} estimated from XPS analysis.

^d d-band center values of Pd atom calculated from PDOS of Pd and Pd₃X slab models in DFT calculation.

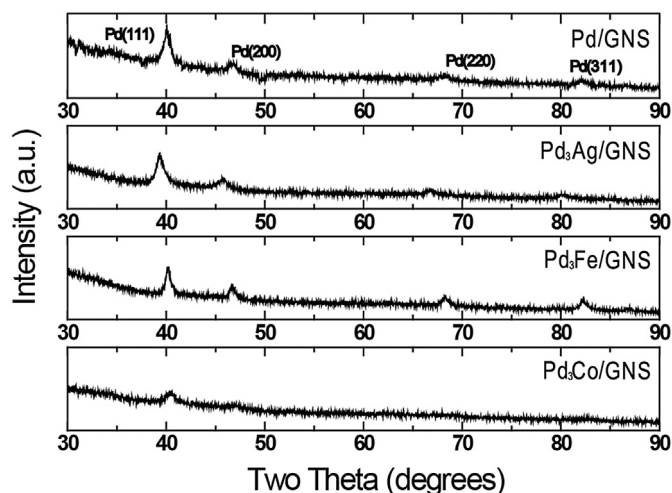


Fig. 2. XRD patterns of the Pd, Pd₃Ag, Pd₃Fe and Pd₃Co nanoparticles supported on GNS.

comparison to our previously reported work [11,40], Pd/GNS, which was heat-treated at 250 °C with 4% H₂ in N₂ gas, exhibits a narrower average particle size (ca. 2 nm) and a decrease in the lattice constant.

3.2. Surface characterization with XPS for Pd/GNS and Pd₃X/GNS

The XPS analyses have been employed to explain the surface oxidation state of the prepared GNS supported nanoparticles. The BE shift estimated using XPS is a fine finger print with respect to the change in the center of the occupied d-states [64,66–68]. The d-band center is strongly related to changes in the catalyst's surface bond energy and the species adsorbed on the surface [42]. This model has been used to understand why the alteration of electronic structures can considerably change catalytic properties [20,23,42]. The core-level BEs of Pd/GNS treated at 573 K (in Fig. 3) observed at approximately 335.3 and 340.5 eV for the major spin–orbit split doublet (Pd 3d_{5/2} and Pd 3d_{3/2}), respectively, which are associated with zero-valent Pd (Pd⁰) [66,69,70]. Another doublet of BEs with respect to Pd 3d_{5/2} and 3d_{3/2} peaks are estimated to be approximately 336.7 and 342.0 eV, attributed to higher oxidation state

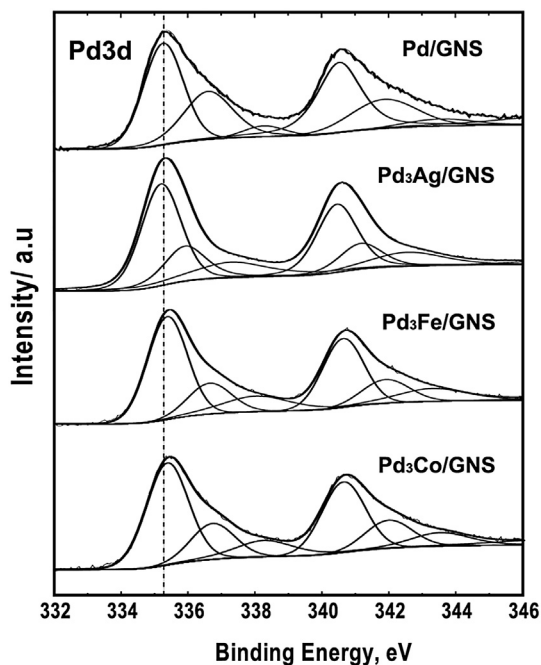


Fig. 3. Pd 3d core-level spectra of the GNS-supported Pd, Pd₃Ag, Pd₃Co and Pd₃Fe in XPS analyses.

close to that of PdO [66,70]. The Pd 3d_{5/2} BEs of Pd₃Ag, Pd₃Fe and Pd₃Co nanoparticles supported on GNS are found to be at 335.2, 335.4 and 335.4 eV, respectively (see Table 1). The peak positions of the presence of metallic Pd are positively or negatively shifted as d–d orbital hybridization arises between Pd and the second metal [66,67]. The Pd 3d_{5/2} BEs of Pd₃Co/GNS and Pd₃Fe/GNS are estimated to shift to higher BEs with respect to Pd/GNS, whereas these of Pd₃Ag/GNS are shifted to lower BEs. These shifts in BE are shown to be consistent with theoretical predictions of the change in the d-band center value as further described below.

3.3. Ab-initio calculation of Pd and Pd₃X surface models

The d band center model assumes that adsorption energy of adsorbed chemical species (e.g., oxygen) on the catalyst surface is strongly correlated to the average weight of the d-band electron energies (d-band center) of a catalyst [23,42,45,71]. Prior to the relaxation of Pd and Pd₃X (X: Ag, Co and Fe) surface, the bulk structures of Pd, Pd₃Ag, Pd₃Fe and Pd₃Co are completely relaxed to find their ground states under vacuum conditions. Afterward, the (2 × 2) surface of Pd, Pd₃Ag, Pd₃Fe and Pd₃Co is generated with six-layer slab model as shown in Fig. 4. From the projected density of states (PDOS) of Pd atom, d band center values of Pd on the surface of Pd and Pd alloys are estimated using Eq. (1) [72].

$$\epsilon_d = \frac{\int_{-\infty}^{E_F} E p_d(E) dE}{\int_{-\infty}^{E_F} p_d(E) dE} \quad (1)$$

Here, ϵ_d is d-band center weight. p_d is the projected density of states onto the d band of a Pd atom. The d-band center value of the Pd atom is evaluated to be –1.82 eV, which is consistent with the results reported in the literature. Likewise, the d-band center values of Pd₃Ag, Pd₃Fe and Pd₃Co alloy are calculated to

be –1.69, –2.21 and –2.15 eV, respectively. The ϵ_d of Pd₃Fe and Pd₃Co are downward shifted than that of pure Pd, whereas that of Pd₃Ag is upward shifted with respect to pure Pd. This trend well matches the core level shift of Pd 3d orbital observed in the XPS results. Based on this fundamental observation, Pd alloys with downward shifted ϵ_d relative to pure Pd metal are likely associated with having relatively weaker bonding with oxygen, thereby leading to better ORR activities [20,44–47,71].

3.4. Rotating-disk electrode studies of Pd and Pd alloys supported on GNS for the oxygen reduction reaction (ORR)

Fig. 5 demonstrates typical CVs of GNS-supported Pd, Pd₃Ag, Pd₃Co and Pd₃Fe, which were obtained using a half-cell system at a scan rate of 50 mV s^{–1} over a potential range of 0.0–1.2 V vs. RHE. The electrochemical active surface (EAS) areas of Pd/GNS, Pd₃Ag/GNS, Pd₃Co/GNS and Pd₃Fe/GNS are estimated from the obtained CVs by assuming that the charge density of an oxygen monolayer on the Pd surface is 405 μC cm^{–2} in the oxygen adsorption and desorption regions [73]. The fully activated EAS areas of Pd/GNS, Pd₃Ag/GNS, Pd₃Fe/GNS and Pd₃Co/GNS are 30.5, 29.2, 30.7, and 40.5 m² g^{–1}, respectively, as summarized in Table 2. As shown in Fig. 6, the rotating-disk electrode (RDE) technique was employed to examine the reaction kinetics at steady state conditions for the ORR [74–76] of Pd/GNS and Pd₃X/GNS as oxygen is reduced to water during the positive sweep at a rotating speed of 1600 rpm in O₂-saturated 0.1 M NaOH and 0.1 M HClO₄ solutions. Based on RHE, the ORR kinetics in alkaline condition is faster than that in acidic condition, as observed by more positive half wave potential, consistent with previously reported results [77,78]. The kinetic currents with respect to the diffusion and activation, are estimated by the following equation [74]:

$$\frac{1}{i} = \frac{1}{i_k} + \frac{1}{i_d} + \frac{1}{i_f} = \frac{1}{i_k} + \frac{1}{BC_0\omega^{1/2}} + \frac{\delta_f}{nF C_f D_f} \quad (2)$$

where i is the current at specific potential within the mixed kinetics–diffusion control region of the ORR polarization curves, i_k is the kinetic current evaluated by equation (2), i_d is the limited diffusion current, i_f is a diffusion current governed by diffusion of oxygen molecules in the film, and B is the Levich constant. C_f and D_f indicate the solubility and the diffusion coefficient of the reactant in the Nafion film. δ_f is the thickness of Nafion, respectively. The j_k values are summarized in Table 2, evaluated for Pd, Pd₃Ag, Pd₃Fe and Pd₃Co nanoparticles supported on GNS in both acidic and alkaline media. In the acidic media, j_k values of Pd₃Fe/GNS (1.26 mA cm^{–2}), and Pd₃Co/GNS (0.93 mA cm^{–2}) are found to be higher than that of the Pd/GNS (0.75 mA cm^{–2}), whereas that of Pd₃Ag/GNS (0.10 mA cm^{–2}) exhibits lower value at the potential of 0.85 V vs. RHE as shown in Fig. 6 and Table 2. Based on the XPS results shown in Fig. 3, the Pd 3d_{5/2} core levels for Pd₃Fe/GNS and Pd₃Co/GNS are changed to higher BE with regards to Pd/GNS, results in a downshift of the d-band center. The lower-shifted d-band center with respect to Pd in an alloy leads to faster kinetics than Pd as a result of smaller vacancy of the d-band of Pd, indicative of a weak Pd–O bond [20]. The results are consistent with former reports which have elucidated the d-bands of Pd by using the d-band center model [23,42,67,79]. In alkaline condition, however, j_k values of GNS-supported Pd₃Ag (7.5 mA cm^{–2}), Pd₃Fe (3.4 mA cm^{–2}), and Pd₃Co (7.2 mA cm^{–2}) alloy catalysts are all lower than that of Pd/GNS (14.3 mA cm^{–2}), at the potential of 0.85 V vs. RHE.

The ORR diffusion limited current increases with the rotation rate and is proportional to the square root of the rotation rate as shown in Fig. 7. The plots in Fig. 7 are known as Koutecky–Levich plots [50,80] and are calculated on the following equation:

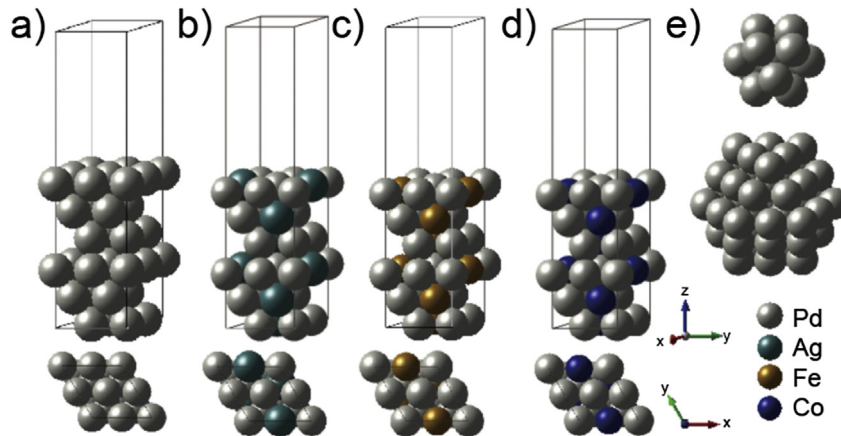


Fig. 4. Top and side view of six-layer (2×2) slab models for each unit cell on the (111) surface of (a) Pd, (b) Pd₃Ag, (c) Pd₃Fe, (d) Pd₃Co and (e) nanoparticle of Pd₁₃ and Pd₅₅.

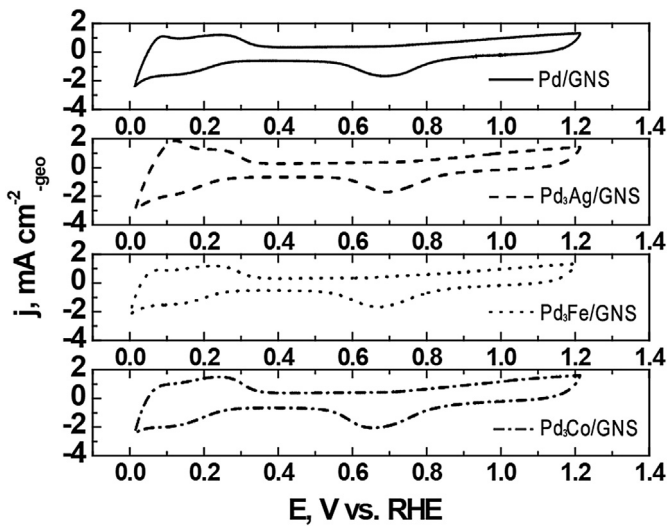
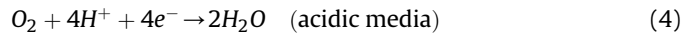


Fig. 5. Cyclic voltammograms of GNS-supported Pd, Pd₃Ag, Pd₃Fe and Pd₃Co catalysts in a 0.1 M HClO₄ electrolyte at a 50 mV s⁻¹ scan rate at room temperature, in which the current densities are normalized to the geometric surface area of the glassy carbon electrode (ca. 0.196 cm²).

$$j_d = 0.62n_eFD^{2/3}\nu^{-1/6}c_0\omega^{1/2} = BC_0\omega^{1/2} \quad (3)$$

where n_e is the transferred number of electrons per O₂ molecules, F is the Faraday constant, D is the diffusion coefficient of dissolved O₂ in electrolyte, ν is the kinematic viscosity of the solution, ω is the rotating speed, and c_0 is the concentration of dissolved O₂ in

electrolyte. The ORR has two major possible pathways by a multi-electron reaction, in which one is associated with the two electron pathway to generate hydrogen peroxide, H₂O₂, and the other is with the transfer of four electrons to produce H₂O and OH⁻ in acidic and alkaline condition, as expressed by the following Eqs. (4) and (5), respectively [81]:



For the ORR of Pd and Pd alloy nanoparticles on GNS, the n_e is estimated to be around 4 from the analysis of the Levich–Koutecky plots, indicative of production of water and hydroxide as reaction products in O₂-saturated acidic and alkaline electrolytes, respectively, as summarized in Table 2. In alkaline conditions, GNS-supported Pd₃X alloy catalysts exhibit relatively lower n_e values, which indicate that they are involved in the two electron pathway to generate H₂O₂. However, Pd₃Fe/GNS and Pd₃Co/GNS, which exhibit better activity in acidic conditions than Pd/GNS, involve n_e of approximately four. In summary, the ORR activity of high loading Pd and Pd alloys on GNSs is ordered in the sequence of Pd/GNS > Pd₃Ag/GNS > Pd₃Co/GNS > Pd₃Fe/GNS in the alkaline condition and in order of Pd₃Fe/GNS > Pd₃Co/GNS > Pd/GNS > Pd₃Ag/GNS in the acidic condition. The differences in ORR remain as an open question. Jiang et al. have reported better performance of Pd/C compared with Pt/C with a high-lying d-band center, and they concluded that the ORR is more suitable on a clean Pd surface than on a pure Pt surface depending on the specific particle size contrary to Pt being more favorable in acidic conditions [27]. Additionally, Lima et al. have observed high ORR

Table 2
Electrochemical parameters of Pd/GNS and Pd₃X/GNS (X: Ag, Co and Fe) catalysts characterized using electrochemical analyses.

Catalysts	Real active surface area (cm ²) ^a	Active surface area (m ² g ⁻¹) ^a	Kinetic current density @ 0.85 vs RHE, j_k (mA cm ⁻²) ^b		Number of electrons transferred, n_e	
			Acid	Alkaline	Acid	Alkaline
60 wt.% Pd/GNS	2.39	30.5	0.75	14.3	3.98	4
67 wt.% Pd ₃ Ag/GNS	2.29	29.2	0.10	7.5	3.44	3.41
64 wt.% Pd ₃ Fe/GNS	2.41	30.7	1.26	3.4	3.87	3.49
64 wt.% Pd ₃ Co/GNS	3.17	40.5	0.93	7.2	3.80	3.26

^a Active surface area calculated with charge of 405 μC cm⁻² estimated by assuming reduction of the monolayer PdO.

^b j_k normalized from surface area of glassy carbon electrode, 0.196 cm⁻².

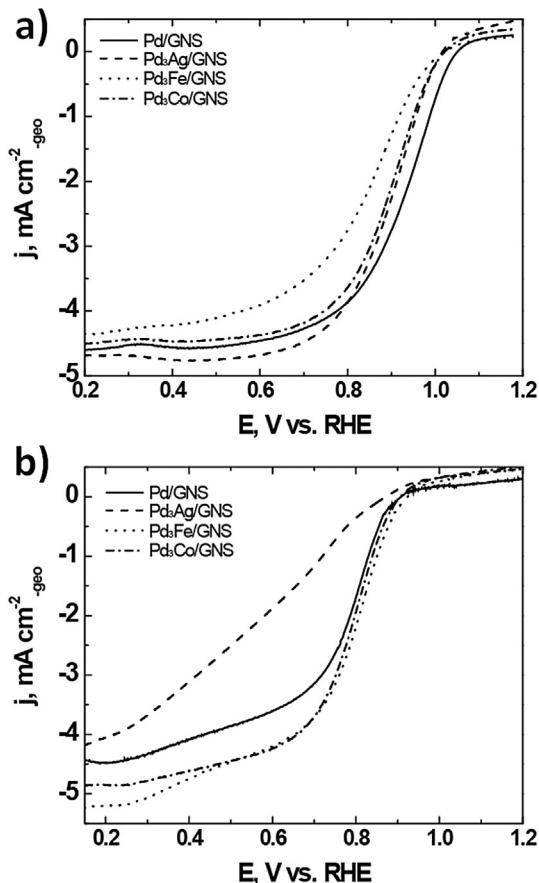


Fig. 6. Comparison of the polarization curves of Pd/GNS and Pd₃X/GNS (X: Ag, Fe and Co) for the ORR in O₂-saturated (a) 0.1 M NaOH and (b) 0.1 M HClO₄ solutions with a sweep rate of 10 mV s⁻¹ at room temperature; rotation speed: 1600 rpm.

activity for Pd(111) in alkaline media that is comparable with that of Pt(111) [82]. Even in our previous work, 60 wt.% Pd/GNS demonstrated a mass- and surface-normalized activity better than that of 60 wt.% Pt/GNS [11]. Several reports have tried to explain such differences through particle size effect [27,82]. However, based on the results presented in previous reports, it is still not sufficient to explain the correlation between the ORR activity and the acidity of the electrolyte as observed by inconsistent ORR activity obtained by similar average particle sizes of Pd and Pd alloy catalysts supported on GNS. On the other hand, recently, N. Ramaswamy et al. have pointed out experimentally the ORR reaction mechanisms for multi-electron transfer through the investigation of ORR activity on carbon supported Pt (Pt/C) in 0.1 M NaOH and 0.1 M HClO₄ electrolyte [83,84]. They proposed that the presence of adsorbed hydroxide species by water dissociation prevents the direct adsorption of molecular O₂ on the active site in acidic solution, whereas an outer-sphere electron transfer mechanism in alkaline media is possible to make the hydroxide intermediates as the product in outer Helmholtz plane (OHP), indicating that peroxide intermediate formed during ORR could instantly carry out the four electron ORR process [83,84]. This explanation supports the inconsistent ORR activity observed with GNS-supported Pd and Pd-based catalysts in acidic and alkaline media, which is ascribed to the possibility of reaction in the OHP. The d-band center values are in good consistency with experimental ORR results in acidic media since the ab-initio computational calculation only considers the reaction in the inner Helmholtz plane (IHP).

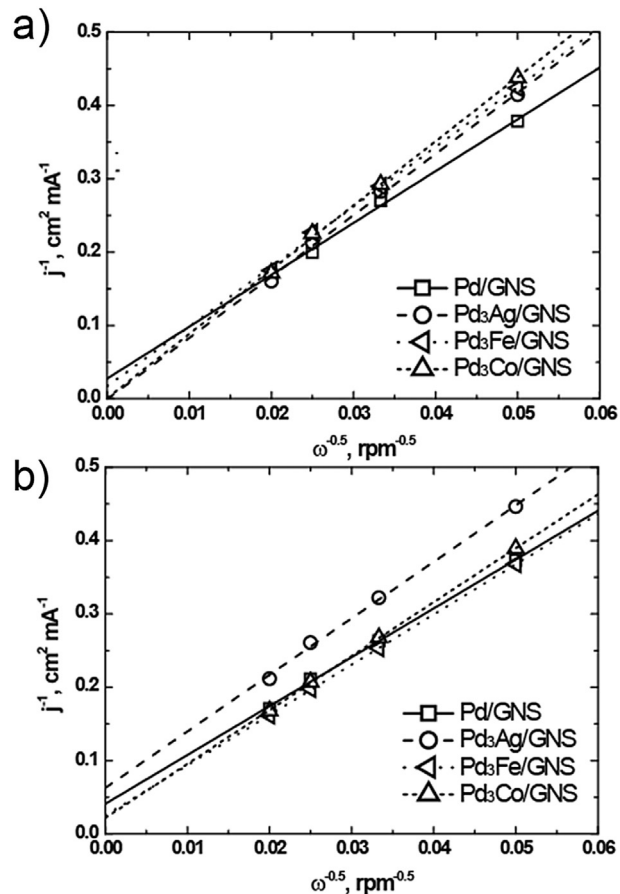


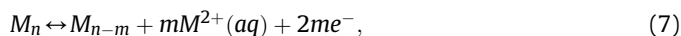
Fig. 7. Levich-Koutecky plots of the ORR collected for Pd/GNS and Pd₃X/GNS (X: Ag, Fe and Co) under (a) alkaline and (b) acidic conditions.

3.5. The first principle study of Pd dissolution potential and cohesive energy

Despite high kinetic activity and cost benefits over state of the art Pt catalysts, Pd based catalysts have not been used in the cathode of the most widely used acidic electrolyte PEMFC due to its inferior electrochemical instability compared to Pt [12,24,85]. The fundamental understanding of the stability issues of Pd based catalysts would be essential in order to further optimize the catalyst design and enhance their catalytic activity. To investigate its stability, the cohesive energy, E_{coh} , and dissolution potential, U_m , have been calculated for both bulk size and nano-sized particles of Pd₁₃ (13 Pd atoms and 0.5 nm in diameter) and Pd₅₅ (55 Pd atoms and 1.1 nm in diameter), respectively, as shown in Fig. 4e by the following Eqs. (6)–(9) based on DFT design of Fig. 4e and our previous reports [4,86–88]:

$$E_{\text{coh}} = -\frac{E_M - nE_{M,g}}{n}, \quad (6)$$

where E_M and $E_{M,g}$ are the DFT energies of bulk and gas in vacuum for Pt or Pd. n is number of Pt or Pd atoms. The dissolution potentials of Pt or Pd have been calculated based on electrochemical dissolution reaction of Eq. (7);



where M is Pt or Pd. The Gibbs free energy for dissolution and

dissolution potentials of Pd or Pt can be expressed by follows Eqs. (8) and (9);

$$\Delta G = \mu^\circ(M_{n-m}) + m \left\{ \mu^\circ(M^{2+}, aq) + kT \ln(a_{M^{2+}}) \right\} - 2meU_m - \left\{ \mu^\circ(M_{n,s}) + kT \ln(a_{M_n}) \right\} \quad (8)$$

$$U_m = U_{bulk} + \frac{1}{2me} \{ mE(M_{bulk}) + E(M_{n-m}) - E(M_n) \}, \quad (9)$$

where μ is the chemical potentials, k is the Boltzmann constant, a is the activity coefficient, and T is the temperature. U_m and U_{bulk} are the dissolution potentials of the outermost M shell and bulk, respectively. Increased E_{coh} indicates an improved electrochemical stability with higher U_m [4,87–89]. The U_{bulk} and E_{coh} for Pd bulk are 0.81 V vs. SHE (e.g., Standard Hydrogen Electrode) and 3.74 eV, respectively. The U_m of Pd₁₃ and Pd₅₅ nanoparticle in DFT design was evaluated to be 0.16 and 0.49 V vs. SHE, respectively, and the E_{coh} was 2.26 and 2.91 eV. These results indicate that bigger particles have higher dissolution potential and cohesive energy, leading to superior electrochemical stability. Therefore, the results obviously demonstrate that Pd nanoparticle even including bulk size Pd can spontaneously dissolve in working potentials at the cathode of PEMFC generally operated between 0.6 and 1.23 V vs. SHE. In AEMFCs condition, which typically operate below 0.4 V vs. SHE at the cathode, on the other hand, Pd nanoparticles with diameter above ca. 1.1 nm is thermodynamically stable. These results reveal that Pd based catalysts might be challenging to use in PEMFCs but acceptable for AEMFCs with respect to stability. Nevertheless, we believe even Pd based catalysts need further study in order to be used in PEMFC through the optimization of electronic structure with suitable method such as employing supports, since we have demonstrated the possibility of increasing U_m and E_{coh} of Pt nanoparticles with small sizes on heteroatom doped carbon based materials with superior electrochemical stability [4,86,88].

4. Conclusions

In this work, GNS support is prepared via thermal exfoliation of GO obtained by the modified Hummers method. GNS-supported Pd, Pd₃Ag, Pd₃Fe and Pd₃Co nanoparticles are then synthesized by the impregnation method coupled with a heat treatment under hydrogen gas. The uniformly dispersed Pd and Pd alloy nanoparticles with an average diameter of ca. 5 nm are well distributed on GNS support with loadings up to 60 wt.%. These catalysts with similar metal particle sizes are used to compare the ORR activity in acidic and alkaline conditions. The Pd 3d_{5/2} core levels for Pd₃Fe/GNS and Pd₃Co/GNS are observed to shift to a higher BE with respect to Pd/GNS, whereas that of Pd₃Ag/GNS shifts to a lower BE. The electrochemical testing results demonstrate that the ORR activity of the high loading Pd and Pd alloy catalysts on GNS is ordered in the sequence of Pd/GNS > Pd₃Ag/GNS > Pd₃Co/GNS > Pd₃Fe/GNS in the alkaline condition, and in the sequence of Pd₃Fe/GNS > Pd₃Co/GNS > Pd/GNS > Pd₃Ag/GNS in acidic condition. Based on these results, the d-band center model is consistent for the ORR activity in acidic condition, whereas a clear trend has not been identified in alkaline condition as demonstrated by Pd/GNS exhibiting better performance than Pd alloy catalysts in alkaline conditions. The prepared GNS-supported Pd and Pd alloy nanoparticle catalysts have shown reliable ORR catalytic activity in acidic and alkaline conditions, suggesting that it may potentially replace Pt for use in cathodes of PEMFC and AEMFC on the basis of kinetic activity. In spite of this, the thermodynamic instability of Pd based catalysts must be addressed before their use in acidic

electrolyte PEMFCs based on the DFT calculation of U_m of Pd₁₃ and Pd₅₅ nanoparticles, where Pd nanoparticles above ca. 1.1 nm in diameter can be utilized under AEMFC operating conditions. For further catalyst design for PEMFC, the thermodynamic stability of Pd based catalysts must be enhanced through the use of advanced supports (e.g., metal oxides and hetero-atom doped carbon-based materials) which could optimize the electronic structure of Pd.

Acknowledgments

This work was financially supported by the Natural Sciences and Engineering Research Council of Canada (NSERC), the Canada Research Chairs Program and the University of Waterloo. This research was also enabled by the National Research Foundation of Korea (NRF) grant funded by the Korea government (MSIP) (No. 2014R1A2A1A11052414) and by the Core Technology Development Program for Next-generation Solar Cells of Research Institute for Solar and Sustainable Energies (RISE), GIST and the New & Renewable Energy Core Technology Program of the Korea Institute of Energy Technology Evaluation and Planning (KETEP), granted financial resource from the Ministry of Trade, Industry & Energy, Republic of Korea (No. 20143010031770).

References

- [1] W. Vielstich, A. Lamm, H.A. Gasteiger, *Handbook of Fuel Cells Fundamentals Technology and Applications*, John Wiley & Sons Ltd., London, 2003.
- [2] K.A. Kuttyiyel, K. Sasaki, Y. Choi, D. Su, P. Liu, R.R. Adzic, *Energy Environ. Sci.* 5 (2012) 5297.
- [3] L. Tang, B. Han, K. Persson, C. Friesen, T. He, K. Sieradzki, G. Ceder, *J. Am. Chem. Soc.* 132 (2010) 596–600.
- [4] M.H. Seo, S.M. Choi, E.J. Lim, I.H. Kwon, J.K. Seo, S.H. Noh, W.B. Kim, B. Han, *ChemSusChem* 7 (2014) 2609–2620.
- [5] M. Winter, R.J. Brodd, *Chem. Rev.* 104 (2004) 4245–4269.
- [6] H.A. Gasteiger, J.E. Panels, S.G. Yan, *J. Power Sources* 127 (2004) 162–171.
- [7] S.M. Choi, M.H. Seo, H.J. Kim, W.B. Kim, *Carbon* 49 (2011) 904–909.
- [8] K.C. Neyerlin, W. Gu, J. Jorne, H.A. Gasteiger, *J. Electrochem. Soc.* 154 (2007) B631–B635.
- [9] S.M. Choi, M.H. Seo, H.J. Kim, E.J. Lim, W.B. Kim, *Int. J. Hydrog. Energy* 35 (2010) 6853–6862.
- [10] M.H. Seo, S.M. Choi, H.J. Kim, J.H. Kim, B.K. Cho, W.B. Kim, *J. Power Sources* 179 (2008) 81–86.
- [11] M.H. Seo, S.M. Choi, H.J. Kim, W.B. Kim, *Electrochem. Commun.* 13 (2011) 182–185.
- [12] M.H. Seo, E.J. Lim, S.M. Choi, H.J. Kim, W.B. Kim, *Top. Catal.* 53 (2010) 678–685.
- [13] N.P. Subramanian, X. Li, V. Nallathambi, S.P. Kumaraguru, H. Colon-Mercado, G. Wu, J.-W. Lee, B.N. Popov, *J. Power Sources* 188 (2009) 38–44.
- [14] R. Bashyam, P. Zelenay, *Nature* 443 (2006) 63–66.
- [15] F. Bidault, D.J.L. Brett, P.H. Middleton, N.P. Brandon, *J. Power Sources* 187 (2009) 39–48.
- [16] J.S. Park, S.H. Park, S.D. Yim, Y.G. Yoon, W.Y. Lee, C.S. Kim, *J. Power Sources* 178 (2008) 620–626.
- [17] K. Asazawa, K. Yamada, H. Tanaka, A. Oka, M. Taniguchi, T. Kobayashi, *Angew. Chem.* 119 (2007) 8170–8173.
- [18] M. Oezaslan, F. Hasche, P. Strasser, *J. Electrochem. Soc.* 159 (2012) B444–B454.
- [19] M.H. Shao, K. Sasaki, R.R. Adzic, *J. Am. Chem. Soc.* 128 (2006) 3526–3527.
- [20] M.H. Shao, T. Huang, P. Liu, J. Zhang, K. Sasaki, M.B. Vukmirovic, R.R. Adzic, *Langmuir* 22 (2006) 10409–10415.
- [21] S. Zhang, X. Yuan, H. Wang, W. Mérida, H. Zhuc, J. Shen, S. Wu, J. Zhang, *Int. J. Hydrog. Energy* 34 (2009) 388–404.
- [22] E. Antolini, J.R.C. Salgado, M.J. Giz, E.R. Gonzalez, *Int. J. Hydrog. Energy* 30 (2005) 1213–1220.
- [23] M.H. Shao, P. Liu, J. Zhang, R.R. Adzic, *J. Phys. Chem. B* 111 (2007) 6772–6775.
- [24] M. Pourbaix, *Atlas of Electrochemical Equilibria in Aqueous Solutions*, National Association of Corrosion Engineers, the University of Michigan, 1974.
- [25] W. Vielstich, A. Lamm, H.A. Gasteiger, *Handbook of Fuel Cells Fundamentals Technology and Applications*, John Wiley & Sons Ltd., London, 2003.
- [26] Y.C. Wei, C.W. Liu, Y.W. Chang, C.M. Lai, P.Y. Lim, L.D. Tsai, K.W. Wang, *Int. J. Hydrog. Energy* 35 (2010) 1864–1871.
- [27] L. Jiang, A. Hsu, D. Chu, R. Chen, *J. Electrochem. Soc.* 156 (2009) B370–B376.
- [28] L. Jiang, A. Hsu, D. Chu, R. Chen, *Electrochim. Acta* 55 (2010) 4506–4511.
- [29] H. Liu, C. Song, L. Zhang, J. Zhang, H. Wang, D.P. Wilkinson, *J. Power Sources* 155 (2006) 95.
- [30] A. Peigney, C. Laurent, E. Flahaut, R.R. Bacsa, A. Rousset, *Carbon* 39 (2001) 507–514.

- [31] A.K. Geim, K.S. Novoselov, *Nat. Mater.* 6 (2007) 183–191.
- [32] K.S. Novoselov, A.K. Geim, S.V. Morozov, D. Jiang, M.I. Katsnelson, I.V. Grigorieva, S.V. Dubonos, A.A. Firsov, *Nature* 438 (2005) 197–200.
- [33] K.I. Bolotin, K.J. Sikes, Z. Jiang, M. Klima, G. Fudenberg, J. Hone, P. Kim, H.L. Stormer, *Solid State Commun.* 146 (2008) 351–355.
- [34] C. Soldano, A. Mahmood, E. Dujardin, *Carbon* 48 (2010) 2127–2150.
- [35] S.M.S. Kumar, J.S. Herrero, S. Irusta, K. Scott, *J. Electroanal. Chem.* 647 (2010) 211–221.
- [36] Y.Y. Shao, G.P. Yin, Y.Z. Gao, *J. Power Sources* 171 (2007) 558–566.
- [37] B. Avsarala, R. Moore, P. Haldar, *Electrochim. Acta* 55 (2010) 4765–4771.
- [38] S. Maass, F. Finsterwalder, G. Frank, R. Hartmann, C. Merten, *J. Power Sources* 176 (2008) 444–451.
- [39] K. Gotoh, K. Kawabata, E. Fujii, K. Morishige, T. Kinumoto, Y. Miyazaki, H. Ishida, *Carbon* 47 (2009) 2112–2142.
- [40] S.M. Choi, M.H. Seo, H.J. Kim, W.B. Kim, *Synth. Met.* 161 (2011) 2405–2411.
- [41] M.H. Seo, S.M. Choi, J.K. Seo, S.H. Noh, W.B. Kim, B. Han, *Appl. Catal. B Environ.* 129 (2013) 163–171.
- [42] B. Hammer, J.K. Nørskov, *Nature* 376 (1995) 238–240.
- [43] B. Hammer, J.K. Nørskov, *Surf. Sci.* 343 (1995) 211–220.
- [44] U.B. Demirci, *J. Power Sources* 173 (2007) 11–18.
- [45] M. Shao, K. Sasaki, N.S. Marinkovic, L. Zhang, R.R. Adzic, *Electrochem. Commun.* 9 (2007) 2848–2853.
- [46] J. Greeley, M. Mavrikakis, *Nat. Mater.* 3 (2004) 810–815.
- [47] J. Greeley, I.E.L. Stephens, A.S. Bondarenko, T.P. Johansson, H.A. Hansen, T.F. Jaramillo, J. Rossmeisl, I. Chorkendorff, J.K. Nørskov, *Nat. Chem.* 1 (2009) 552–556.
- [48] N.I. Kovtyukhova, P.J. Ollivier, B.R. Martin, T.E. Mallouk, S.A. Chizhik, E.V. Buzaneva, A.D. Gorchinskiy, *Chem. Mater.* 11 (1999) 771–778.
- [49] T.J. Schmidt, H.A. Gasteiger, G.D. Stab, P.M. Urban, D.M. Kolb, R.J. Behm, *J. Electrochem. Soc.* 145 (1998) 2354–2358.
- [50] K.J.J. Mayrhofer, D. Strmcnik, B.B. Blizanac, V. Stamenkovic, M. Arenz, N.M. Markovic, *Electrochim. Acta* 53 (2008) 3181–3188.
- [51] G. Kresse, J. Furthmüller, *Phys. Rev. B* 54 (1996) 11169.
- [52] P. Hohenberg, W. Kohn, *Phys. Rev.* 136 (1964) B864–B871.
- [53] W. Kohn, L.J. Sham, *Phys. Rev. A* 140 (1965) 1133–1138.
- [54] G. Kresse, D. Joubert, *Phys. Rev. B* 59 (1999) 1758.
- [55] P.E. Blöchl, *Phys. Rev. B* 50 (1994) 17953.
- [56] J.P. Perdew, K. Burke, M. Ernzerhof, *Phys. Rev. Lett.* 77 (1996) 3865.
- [57] J.P. Perdew, K. Burke, Y. Wang, *Phys. Rev. B* 54 (1996) 16533–16539.
- [58] G. Kresse, J. Furthmüller, *Comput. Mater. Sci.* 6 (1996) 15–50.
- [59] M. Methfessel, A.T. Paxton, *Phys. Rev. B* 40 (1989) 3616–3621.
- [60] E. Antolini, *Appl. Catal. B Environ.* 88 (2009) 1–24.
- [61] J. Perez, E.R. Gonzalez, E.A. Ticianelli, *Electrochim. Acta* 44 (1998) 1329–1339.
- [62] L. Genies, R. Faure, R. Durand, *Electrochim. Acta* 44 (1998) 1317–1327.
- [63] E. Antolini, *Mater. Chem. Phys.* 78 (2003) 563–573.
- [64] J.H. Kim, S.M. Choi, S.H. Nam, M.H. Seo, S.H. Choi, W.B. Kim, *Appl. Catal. B Environ.* 82 (2008) 89–102.
- [65] F.J. Nores-Pondal, I.M.J. Vilella, H. Troiani, M. Granada, S.R.d. Miguel, O.A. Scelza, H.R. Corti, *Int. J. Hydrog. Energy* 34 (2009) 8193–8203.
- [66] K. Lee, O. Savadogo, A. Ishihara, S. Mitsushima, N. Kamiya, K.I. Otac, *J. Electrochem. Soc.* 153 (2006) A20–A24.
- [67] M. Wakisaka, S. Mitsui, Y. Hirose, K. Kawashima, H. Uchida, M. Watanabe, *J. Phys. Chem. B* 110 (2006) 23489–23496.
- [68] H.J. Kim, Y.S. Kim, M.H. Seo, S.M. Choi, W.B. Kim, *Electrochem. Commun.* 11 (2009) 446–449.
- [69] A.V. Naumkin, A. Kraut-Vass, S.W. Gaarenstroom, C.J. Powell, , National Institute of Standards and Technology, Gaithersburg, 2000.
- [70] I.G. Casella, M. Contursi, *J. Electroanal. Chem.* 588 (2006) 147–154.
- [71] J. Greeley, I.E.L. Stephens, A.S. Bondarenko, T.P. Johansson, H.A. Hansen, T.F. Jaramillo, J. Rossmeisl, I. Chorkendorff, J.K. Nørskov, *Nat. Chem.* 1 (2009) 552–556.
- [72] P. Kratzer, B. Hammer, J.K. Nørskov, *J. Chem. Phys.* 105 (1996) 5595–6005.
- [73] H.C. Schniepp, J.L. Li, M.J. McAllister, H. Sai, M. Herrera-Alonso, D.H. Adamson, R.K. Prud'homme, R. Car, D.A. Saville, I.A. Aksay, *J. Phys. Chem. B* 110 (2006) 8535–8539.
- [74] N.M. Markovic, B.N. Grgur, P.N. Ross, *J. Phys. Chem. B* 101 (1997) 5405–5413.
- [75] S.J. Yoo, H.Y. Park, T.Y. Jeon, I.S. Park, Y.H. Cho, Y.E. Sung, *Angew. Chem. Int.* 47 (2008) 9307–9310.
- [76] H.A. Gasteiger, N.M. Markovic, P.N. R. Jr., *J. Phys. Chem.* 99 (1995) 8290–8301.
- [77] S. Takenaka, N. Susuki, H. Miyamoto, E. Tanabe, H. Matsunea, M. Kishida, *Chem. Commun.* 46 (2010) 8950–8952.
- [78] L. Jiang, A. Hsu, D. Chu, R. Chen, *J. Electrochem. Soc.* 156 (2009) B643–B649.
- [79] J. Greeley, I.E.L. Stephens, A.S. Bondarenko, T.P. Johansson, H.A. Hansen, T.F. Jaramillo, J. Rossmeisl, I. Chorkendorff, J.K. Nørskov, *Nat. Chem.* 1 (2009) 552–556.
- [80] U.A. Paulus, T.J. Schmidt, H.A. Gasteiger, R.J. Behm, *J. Electroanal. Chem.* 495 (2001) 134–145.
- [81] J. Guo, A. Hsu, D. Chu, R. Chen, *J. Phys. Chem. C* 114 (2010) 4324–4330.
- [82] F.H.B. Lima, J. Zhang, M.H. Shao, K. Sasaki, M.B. Vukmirovic, E.A. Ticianelli, R.R. Adzic, *J. Phys. Chem. C* 111 (2007) 404–410.
- [83] N. Ramaswamy, U. Tylus, Q. Jia, S. Mukerjee, *J. Am. Chem. Soc.* 135 (2013) 15443–15449.
- [84] N. Ramaswamy, S. Mukerjee, *Adv. Phys. Chem.* 2012 (2012) 17.
- [85] R.K. Singh, R. Rahul, M. Neergat, *Phys. Chem. Chem. Phys.* 15 (2013) 13044–13051.
- [86] D. Higgins, M.A. Hoque, M.H. Seo, R. Wang, F. Hassan, J.-Y. Choi, M. Pritzker, A. Yu, J. Zhang, Z. Chen, *Adv. Funct. Mater.* 24 (2014) 4325–4336.
- [87] J.K. Seo, A. Khetan, M.H. Seo, H. Kim, B. Han, *J. Power Sources* 238 (2013) 137–143.
- [88] S.H. Noh, M.H. Seo, J.K. Seo, P. Fischer, B. Han, *Nanoscale* 5 (2013) 8625–8633.
- [89] D. Higgins, F.M. Hassan, M.H. Seo, J.-Y. Choi, M.A. Hoque, D.U. Lee, Z. Chen, *J. Mater. Chem. A* 3 (2015) 6340–6350.